

# MITSuME observation of V404 Cygni in the 2015 outburst: Two optical variable components with different variability

Y. Tachibana<sup>1</sup>, T. Yoshii<sup>1</sup>, H. Hanayama<sup>2</sup>, and N. Kawai<sup>1</sup>

<sup>1</sup>Department of Physics, Tokyo Institute of Technology, 2-12-1, Ohokayama, Tokyo, Japan

<sup>2</sup>Ishigakijima Astronomical Observatory, National Astronomical Observatory of Japan, National Institutes of Natural Sciences, 1024-1 Arakawa, Ishigaki, Okinawa 907-0024, Japan

\*E-mail: tachibana@hp.phys.titech.ac.jp

Received ; Accepted

## Abstract

The black hole binary V404 Cygni (= GS 2023+338) had an outburst on June 15, 2015 after 26 years of quiescence. We report the multi-color optical observation ( $g'$ ,  $R_C$ , and  $I_C$ ) of this object at the beginning of its outburst performed by the *MITSuME* 50cm telescope in Akeno, Yamanashi, and the *MURIKABUSHI* 105 cm Telescope at Ishigakijima Astronomical Observatory. With time domain analysis of the multi-color light curves, we successfully decomposed optical variations into two components: a highly-variable, and a little-variable component. The loci of the little-variable component in the color-color diagram are consistent with that of the multi-temperature blackbody radiation, while those of the highly-variable component trace out a power-law spectrum with a spectral index  $\alpha \sim 0.6$ – $1.0$ . For the little-variable component, we argue that an irradiated disk with the innermost temperature higher than  $\sim 2.0 \times 10^4$  K and the outermost temperature lower than  $\sim 6.5 \times 10^3$  K is the most plausible source. The gradual rise trend of the light curve during our observation is probably due to the growing of the little-variable component. The observed spectral energy distribution (SED) from the optical to ultraviolet can be expressed by a model consisting of a power-law component and an irradiated disk component.

## 1 Introduction

Many stellar-mass black holes are widely known to have a violent X-ray flux oscillation on various time scales from milliseconds to hours. Each time scale being related to different emission origins such as the non-thermal jet, the accretion disk, or the corona; the X-ray fluctuation we can observe is the superposition of them. Some models are proposed to describe the behavior of such objects, included in low mass X-ray binaries (LMXBs); *e.g.*, disk instability model, see Lasota 2001 for a review of the model. Its validity is confirmed for 52 X-ray binaries including 23 black hole binaries mainly based on X-ray flux variations (Coriat et al. 2012).

In optical or infrared range, however, similar variations with X-ray's have been observed in only a few black hole binaries:

GX 339–4 (Motch et al. 1983), GRS 1915+105 (Eikenberry et al. 1998), XTE J1118+480 (Uemura et al. 2000), V4641 Sgr (Uemura et al. 2002), and V404 Cygni (Tanaka et al. 2016, Martí et al. 2016, Gandhi et al. 2016, Kimura et al. 2016). For GX 339–4 and XTE J1118+480, the optical flickering is dozens of per cent of its flux on time-scales of seconds, and the scenario of cyclo-synchrotron emission associated with various magnetic flare scales was proposed by Motch et al. (1983) and Merloni et al. (2000), respectively. On the other hand, the optical variation in V4641 Sgr contains large amplitude variations ( $\sim 1$  mag, corresponding to 150 per cent of its flux) on a time-scale of 0.01–0.10 day along with small flickering ( $\sim 0.2$  mag, corresponding to 20 per cent of its flux) on time-scale of 100–200 s.

V404 Cygni, also known as GS 2023+338, is a black hole binary (BHB), originally discovered during the 1989 outburst by the *GINGA* satellite (Kitamoto et al. 1989, Makino et al. 1989). Since the discovery of V404 Cygni, intensive photometric and spectroscopic follow-up have been performed and yielded well-determined physical parameters of its system; the central black hole mass  $M_{\text{BH}} = 9.0^{+0.2}_{-0.6} M_{\odot}$  with a companion mass  $M_2 = 0.7^{+0.3}_{-0.2} M_{\odot}$  (Khargharia et al. 2010), a parallax distance  $2.39 \pm 0.14$  kpc (Miller-Jones et al. 2009), the inclination angle  $i = 67^{\circ}_{-1}^{+3}$  (Shahbaz et al. 1994), and an orbital period of 6.5 d (Casares et al. 1992).

On 2015 June 15, 2015 (MJD 57188), V404 Cygni had an outburst after 26 years of quiescence. The burst was detected and reported by *Swift*/Burst Alert Telescope (BAT) and consecutively by the Monitor of All-sky Image (*MAXI*) instrument (Barthelmy et al. 2015 and Negoro et al. 2015, respectively). After the notifications, intensive observations with from radio to gamma-ray is performed all around the world.

In contrast to typical blackhole transients having a fast rise and exponential decay profile such as A0620-00 within one X-ray flare (sometimes together with an optical correlated flare), V404 Cygni showed multiple X-ray flaring activity during the outburst (Tanaka and Shibazaki. 1996, Ferrigno et al. 2015). For its spectral characteristics, Natalucci et al. (2015), Rodriguez et al. (2015), and Roques et al. (2015) classified the spectral states into “off-flare” and “on flare”, and they concluded that the origin of the flare component was Comptonization. Based on *INTEGRAL* observations, the X-ray variability is originated in accelerations of electrons and also the variable absorption by absorbers in the line of sight. *Chandra* observations, revealed the detection of emission lines in the spectrum indicating disk wind emission, supporting the existence of such matter (King et al. 2015). Kimura et al. (2016), however, pointed out that the X-ray spectrum does not show a noticeable rise in column density when the X-ray flux sharply dropped. They concluded that absorption cannot be the primary cause of the time variation in their data set. Radhika et al. (2016) analyzed *Swift*/XRT and BAT observations for the 2015 outburst of V404 Cygni. They found that the X-ray spectra exhibited the hard, intermediate, and soft spectral state, and hardness intensity diagram do not show a “q-shape” usually observed in black hole transients (Fender and Belloni 2004). They suggested that spectral change is associated with coronal ejection.

For optical range, the nature of the variation is still under discussion in spite of the well determined physical parameters that would enable us to investigate the physics around the black hole. The scenario that the nature of the optical emission is mainly the outer disk irradiated by X-ray emission generated in the inner disk, is proposed by Kimura et al. (2016) based upon repetitive patterns in the optical variation and spectral energy

distribution (SED) analysis with a quite extensive data set of multi-color optical photometric data, and supported by Muñoz-Darias (2016).

On the other hand, the scenario that relativistic non-thermal emission component with the accretion disk spectrum is proposed by Marti et al. (2016) and Tanaka et al. (2016). Martí et al. (2016) tentatively interpreted the origin of the optical emission by the relativistic plasmons along collimated jets as a result of accretion disk instabilities. Tanaka et al. (2016) had further investigated the origin of the variation based upon modeling of broad-band SED from radio to gamma-ray bands. Gandhi et al. (2016) reported sub-second optical flaring activity in the optical band on MJD 57199 (corresponding to the peak of the outburst) and explained its origin as optically thin synchrotron emission from a jet. Lipunov et al. (2016) and Shahbaz et al. (2016) reported the detection of the change of the polarization ( $\sim 1\text{--}5\%$ ) correlating with optical variability and concluded that the variation of the polarization is yielded from relativistic jet. All of them suggested the existence of either a disc or the other component for the optical emission together with the jet.

In this paper, we present the optical data obtained using a MITSuME instrument and results acquired through spectral-timing analysis. Our aim is to derive information about the nature of the complex optical variation.

## 2 Observations and Data Reductions

A series of intensive optical observations of V404 Cyg were performed with three color imaging system developed for MITSuME project (Kotani et al. 2005, Yatsu et al. 2007, Shimokawabe et al. 2008) on the *MITSuME* 50cm telescope in Akeno and the *MURIKABUSHI* 105cm telescope during the period MJD 57192 – 57207. The system allows us to take simultaneous images in  $g'$ ,  $R_C$ , and  $I_C$ -bands by employing dichroic mirrors. The effective wavelengths of the filters are 4770, 6492, and 8020 Å, respectively (Fukugita et al. 1996). *MITSuME* telescope employs three Apogee Alta U-6 camera, KAF-1001E CCD with  $1024 \times 1024$  active area pixels, and the pixel size is  $1.6 \text{ arcsec pixel}^{-1}$  at the focal plane. It is designed to have a field of view (FOV) of 27.3 arcmin. On the other hand, *MURIKABUSHI* telescope covers a FOV of 12.3 arcmin, and then has a pixel resolution of  $0.72 \text{ arcsec pixel}^{-1}$ .

The obtained raw data were preprocessed in a standard manner; subtracting dark and bias, and then dividing by a flat frame. The pixel coordinates are calibrated into celestial coordinates using WCSTools (Mink 1997). After the primary treatment, we performed aperture photometry to estimate the magnitude of this object by comparing with five local reference stars using IRAF tasks. In order to improve an accuracy in the magnitude estimation of V404 Cyg, the magnitudes of reference stars are calibrated by eleven photometric standard stars selected from

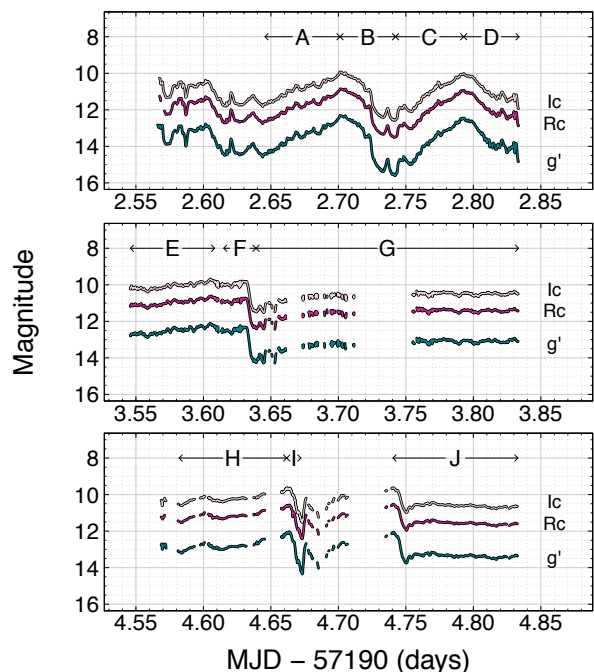


Fig. 1. Observed  $g'$ ,  $R_C$ , and  $I_C$  light curves of V404 Cyg in MJD 57192–57194.

Landolt (1992) and Smith et al. (2002). Information of the reference stars and the standard stars are summarized in Table 1.

In this paper, we focus on the flux variation of V404 Cyg in MJD 57192 – 57194, because during this period we could obtain a higher quality photometric data thanks to good sky condition compared to later observations. We used variable exposures of 5 – 60 sec, chosen to give reasonable count rates for this object in the three bands at different flux levels ( $g' \lesssim 15.5$  mag,  $R_C \lesssim 13.5$  mag, and  $I_C \lesssim 12.5$  mag). A log of the observations is given in Table 2. It should be note that there is a line-of-sight contaminating star at 1.5 arcsec north of V404 Cyg and we could not separate it from V404 Cyg. However, the magnitude of the contamination star is  $g' \sim 19.9$  mag (Shahbaz et al. 2003),  $\sim 60$  times fainter than V404 Cygni at its faintest flux level in this period. We therefore ignored the contamination in our photometry procedures. The time series data of  $g'$ ,  $R_C$  and  $I_C$ -band photometry will be available via Centre de Données astronomiques de Strasbourg (CDS, Strasbourg astronomical Data Center <sup>1</sup>).

### 3 The Light Curve of V404 Cyg

Fig.1 shows the optical ( $g'$ ,  $R_C$ , and  $I_C$ -band) light curves during MJD 57192–57194, corresponding to 4–6 days after the detection of X-ray outburst on MJD 57188. Although we continuously observed V404 Cyg in the optical bands through the night in these observational days, on around MJD 57193.30

or 57194.72, for example, the observation was partially intercepted by clouds resulting in loss of data.

MJD 57192–57194 being categorized as “gradually rising” phase toward to “plateau” phase (Kimura et al. 2016), we can see that averaged brightness in each band on MJD 57194 (13.2 mag, 11.4 mag, and 10.5 mag in  $g'$ ,  $R_C$ , and  $I_C$ -band, respectively) is brighter about 0.6 mag than that on MJD 57192 (13.7 mag, 12.0 mag, and 11.1 mag in each band, respectively). The amplitudes of flux variations was largest on MJD 57192 reaching  $\sim 3$  mag on a timescale shorter than an hour. Variation on MJD 57192 seems to be composed by two distinct fluctuations; big-slow swings and small-fast wiggles. On the other hand, in MJD 57193 and 57194, fast drops in flux rather than big-slow swings were seen, while small wiggles remained. Throughout the observations, variations with large amplitudes always have longer timescales in rising parts than in the falling parts. For all variations, the fluxes in the optical three bands were always well correlated.

### 4 Screening of Optical Photometric Data

In order to improve accuracy of the analysis, we had screened the optical data using the measurements of magnitudes of two reference stars. First, we discarded low-quality data with  $\sqrt{\sigma_i^2 + \sigma_j^2} \geq 0.25$ , where  $\sigma_i$  or  $\sigma_j$  is the statistical error in calculated magnitude of reference star  $i$  or  $j$ . And next we selected the data whose 99.99% confidence interval (for the normal distribution) of the difference in magnitudes of reference star  $i$  and  $j$ ,  $\Delta M_{ij}$ , including the average of the deference in two reference stars over the all data  $\overline{\Delta M_{ij}}$  with  $|\Delta M_{ij} - \overline{\Delta M_{ij}}| \leq 3.89\sqrt{\sigma_i^2 + \sigma_j^2}$ .

The resulting typical statistical uncertainty in the magnitudes of the reference stars were  $\sim 0.07$ ,  $\sim 0.03$ , and  $\sim 0.04$  mag in  $g'$ ,  $R_C$ , and  $I_C$ -bands in *MITSuME/Akeno*, and  $\sim 0.01$  mag in the all optical bands in the *MURIKABUSHI* Telescope. The error of  $\Delta M_{ij}$  ( $= \sqrt{\sigma_i^2 + \sigma_j^2}$ ) larger than 0.25 was therefore outlier, mainly due to bad sky condition. We iterated the latter treatment until  $\overline{\Delta M_{ij}}$  converged. The data selections are performed for all combinations of reference stars ( ${}_5C_2 = 10$  possible outcomes), and we picked up the data meeting the requirement for the entire twenty combinations. Eventually, about 35% data are discarded by this treatment.

### 5 Analysis and results

#### 5.1 Color-color Diagram

Color-color diagram is helpful to categorize the observed flux variation and to test the applicability of assumed emission models. Belloni et al. (2000), for example, have classified X-ray variation in GRS 1915+105 into twelve separate classes and proposed the emission processes of these variations through

<sup>1</sup> <http://cds.u-strasbg.fr/>

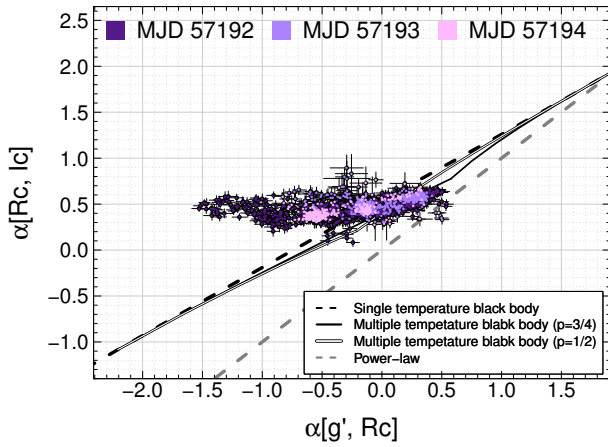


**Fig. 2.** Color-color diagram for the data in Fig.1 with the spectral indices between  $g'$ -band and  $R_C$ -band, and  $R_C$ -band and  $I_C$ -band. Magnitude is converted into energy flux density  $F_\nu$  [erg/s/cm<sup>2</sup>/Hz] using  $A_V = 3.3$  and  $R_V = 2.8$ . The details are written in §5.1.

color-color diagram analysis. We therefore calculated the spectral indices between  $g'$ -band and  $R_C$ -band ( $\alpha_{gr}$ ), and  $R_C$ -band and  $I_C$ -band ( $\alpha_{ri}$ ) for all the data point in Fig.1 and presented them in a color-color diagram (Fig.2). When converting the observed magnitudes to intrinsic fluxes  $F_\nu$ , we adopted  $A_V = 3.3$  and  $R_V = A_V/E(B - V) = 2.8$  among the possible values,  $A_V = 3.0 - 3.6$  (Shahbaz et al. 2003, Hynes et al. 2009, and Itoh et al. 2016) with  $R_V < 3.0$  (Itoh et al. 2016), under the constrain of  $E(B - V) \sim 1.2$  (Itoh et al. 2016; Rahoui et al. 2017). Then the dereddening law described in O'Donnell (1994) was applied for the central frequencies for the three bands:  $3.74 \times 10^{14}$  Hz ( $I_C$ -band),  $4.62 \times 10^{14}$  Hz ( $R_C$ -band), and  $6.28 \times 10^{14}$  Hz ( $g'$ -band). The result is drawn by grey points in Fig.2. The grey dashed line and black dashed line trace loci for power-law spectra with different spectral indices and single temperature black body with different temperatures, respectively, whereas the black line and black-edged white line represents those for standard disk blackbody and irradiated disk blackbody ( $p=3/4$ : Shakura & Sunyaev 1973, and  $p=1/2$ : King & Ritter 1998) for different inner/outer-most temperatures under the condition that the disk temperature cannot across the critical temperature  $\sim 5000K$  where the disk would be unstable (King & Ritter 1998, Życki et al. 1999), respectively. Here,  $p$  is the gradient index of the surface temperature of the accretion disk ( $T$ ) when expressed as a function of the radial distance from the center ( $r$ ); *i.e.*  $T \propto r^{-p}$  (*e.g.* Mineshige et al. 1994). If the optical emission has a power-law spectrum and its variation is attributed to only the change of its normalization, the data points will stay at the same place on the grey dashed line. On the other hand, if the power-law spectrum changes its spectral index, data point move along the grey dashed line. Similarly, points for a blackbody or disk emission model follow the corre-

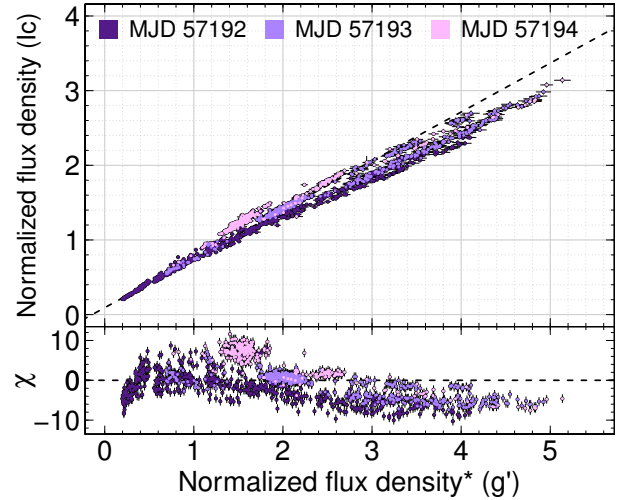


**Fig. 3.** Flux-flux plot with the fluxes between  $g'$ -band and  $I_C$ -band. The details are written in §5.2.

\*In units of  $10^{23}$  erg/cm<sup>2</sup>/s/Hz assuming tentative value  $A_V = 4.0$  and  $R_V = 3.1$ . Note that the absolute value of the flux does not influence our discussion and result.

sponding line if its characteristic temperature changes.

Apparently, the points in the color-color diagram does not trace any of the model lines of the single temperature black body, the multi-temperature black body, or power-law spectra. It indicates that the optical variation cannot be attributed to a single emission component, expressed by single-temperature or multi-temperature blackbody, or power-law model.

## 5.2 Flux-flux Plot

Using the color-color diagram, we showed that the optical variation of V404 Cyg is not attributed to changes of a parameter of a single emission mechanism. In this section, we further investigate the properties of the optical behavior phenomenologically on the flux-flux plot.

Fig.3 shows the flux-flux plot constructed by the  $g'$  and  $I_C$ -band photometric data from MJD 57192 to 57194. Gray scale of each point indicates the date of the observation, as shown in the right bar in MJD, and the dashed line on the upper panel shows the linear fit to all the data, where fitting was performed to minimize the normalized residual defined as follows

$$\chi^2 = \sum_i \frac{[y_i - f(x_i)]^2}{\sigma_{y_i}^2 + [df(x)/dx]_{x_i}^2 \sigma_{x_i}^2}. \quad (1)$$

Here  $(x_i, y_i)$  is the flux data ( $x_i$ :  $g'$ ,  $y_i$ :  $I_C$ ),  $(\sigma_{x_i}, \sigma_{y_i})$  is the corresponding uncertainties, and  $f(x)$  is the function to be fitted. The lower panel shows the normalized residual expressed by

$$\chi_i = \frac{y_i - f(x_i)}{\sqrt{\sigma_{y_i}^2 + [df(x)/dx]_{x_i}^2 \sigma_{x_i}^2}}. \quad (2)$$

Interestingly, in the normalized residual plot, we find a general convex shape and systematic deviations that evolve upward (*i.e.*

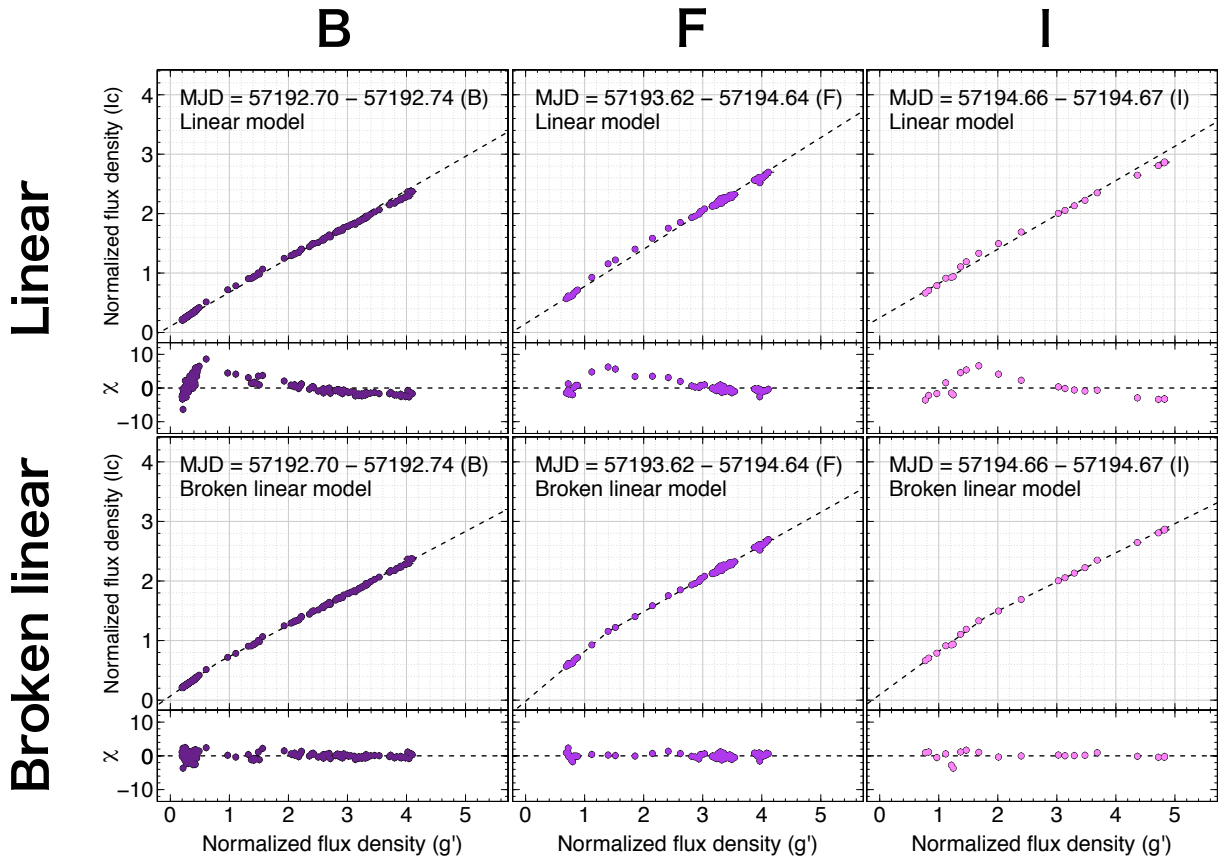


**Fig. 4.** The typical flux-flux plots with the fluxes between  $g'$ -band and  $I_C$ -band. The upper panels are those fitted with a linear model, while the lower panels are fitted with a broken linear model. The details are written in §5.3.

the spectrum gradually reddened as time proceeded) with time. Similar break features were reported in the X-ray flux-flux plots of Seyfert galaxy NGC 4051 (Ponti et al., 2006) and NGC 3227 (Noda et al., 2014). This behavior in the flux-flux plot suggests that the observed optical variation arises from at least two components that are dominant below and above the break. Our result suggests the existence of a multiple engines in optical flux variation of V404 Cygni.

### 5.3 Modeling the convex shape for the Flux-flux Plot

In this section, we test two functional forms to express the convex shape on the flux-flux plot: broken-linear function and power-law function.

When a point  $(F(\nu_1, t), F(\nu_2, t))$  lies on a linear model  $(F(\nu_2, t) = k_{\text{lin}}F(\nu_1, t) + C)$ , the local spectral index of a variable component  $\alpha$  at the two frequencies  $(\nu_1, \nu_2)$  can be directly derived from  $k_{\text{lin}}$ . Using the local spectral index  $\alpha$ ,  $F(\nu_1)$  and  $F(\nu_2)$  can be expressed by

$$\begin{aligned} F(\nu_1, t) &= A(t)\nu_1^\alpha + C(\nu_1) \\ F(\nu_2, t) &= A(t)\nu_2^\alpha + C(\nu_2), \end{aligned} \quad (3)$$

where  $A(t)$  is normalization of the variable component, and  $C(\nu)$  is the spectrum of stable component. Eliminating  $A(t)$ , equations (5.3) are reduced to

$$F(\nu_2, t) = \left(\frac{\nu_2}{\nu_1}\right)^\alpha F(\nu_1, t) + \left[-\left(\frac{\nu_2}{\nu_1}\right)^\alpha C(\nu_1) + C(\nu_2)\right]. \quad (4)$$

One sees that the slope of the linear model on the flux-flux plot is  $(\nu_2/\nu_1)^\alpha$ .

In contrast, if the variable component changes its spectral index, the relationship between  $F(\nu_1, t)$  and  $F(\nu_2, t)$  will not be linear. In particular, if the spectral variability is explained by power-law pivoting (e.g. Taylor et al. 2003, Uttley & McHardy 2005) at a frequency  $\nu_p$ , the data on the flux-flux plot should follow  $F(\nu_2, t) - C(\nu_2) = F_p^{1-\beta} [F(\nu_1, t) - C(\nu_1)]^\beta$ , by reducing variable spectral index  $\alpha(t)$  from

$$\begin{aligned} F(\nu_1, t) &= F_p (\nu_1/\nu_p)^{\alpha(t)} + C(\nu_1) \\ F(\nu_2, t) &= F_p (\nu_2/\nu_p)^{\alpha(t)} + C(\nu_2), \end{aligned} \quad (5)$$

where  $F_p$  is the constant flux at  $\nu_p$  and  $\beta = \log(\nu_2/\nu_p)/\log(\nu_1/\nu_p)$ .

As noted in §5.2, the data distributions in the flux-flux plot apparently do not trace a linear model. We thus tested two convex functional forms to fit the flux-flux plot: broken-linear

model (two linear models connected at a break) and power-law function.

Because the data in the flux-flux plot shows systematical time-dependent evolution, we divided the data to ten sections (A–J in Fig.1) by their rising and declining trends. Note that Fig.1 shows data points before the screening described in §4 is applied. Then we performed fits with broken-linear model represented to

$$y = \begin{cases} k_1 x + C & (x < F_{\text{br}}) \\ k_2 x + (k_1 - k_2)F_{\text{br}} + C & (x \geq F_{\text{br}}), \end{cases} \quad (6)$$

where  $k_1$  and  $k_2$  is the slope of two linear functions, and  $C$  is the intercept of the linear function for the lower flux. All of these four parameters are free. Typical examples of the fitting are shown in Fig.4. The upper and lower panels are the results of fitting with the linear model and the broken-linear model respectively. The three columns are corresponding to the time portions which contain drastic flux declines: MJD = 57192.70 – 57192.74 (B), 57193.61 – 57193.64 (F), and 57194.66 – 57194.67 (I). The linear model fits give  $\chi^2/\text{d.o.f} = 843/140$ , 153/70, and 130/19 for each time periods, whereas the broken-linear model fits give significantly improved values  $\chi^2/\text{d.o.f} = 154/138$ , 34/68, and 30/17.

We next tested the power-law model:  $y = k_{\text{pow}}(x - C_1)^\beta + C_2$ , where  $k_{\text{pow}}$ ,  $\beta$ ,  $C_1$ , and  $C_2$  are free parameters. We found power-law model give consistently worse fit than the broken-linear model for each portion:  $\chi^2/\text{d.o.f} = 180/138$ , 55/68, and 48/17. In addition,  $C_1$  and  $C_2$  changed significantly from a section to another; though they represent the component constant during each section and therefore expected not to change dramatically between different section. We therefore adopt a broken-linear model to express the behavior of the data on the flux-flux plot in this paper.

#### 5.4 Decomposing the Optical Variations

As mentioned in §5.3, the slope of the straight line on a flux-flux plot is directly leads the local spectral index between  $\nu_1$  and  $\nu_2$ . For the optical variation in V404 Cygni, we found that the data in flux-flux plot was well expressed by a broken-linear model (see §5.3 and Fig.4). Two linear branches below and above a break imply that the existence of two variable components with distinct spectral indices.

To derive slopes for two branches, we fitted a broken-linear model to data in entire periods A–J. It must be noted that (1) we used “screened data” explained in §4, (2) we only used portions containing more than 15 data points, and (3) we used a single component linear model for the portions where a break was not prominent. Except for such two portions, MJD = 57193.5459–57193.6083 (E) and 57193.6390–57193.8335 (G), we derived two slopes with broken-linear models. The derived parameters are tabulated in Table 3. Those for the  $g'$  and  $I_C$  pair are plotted

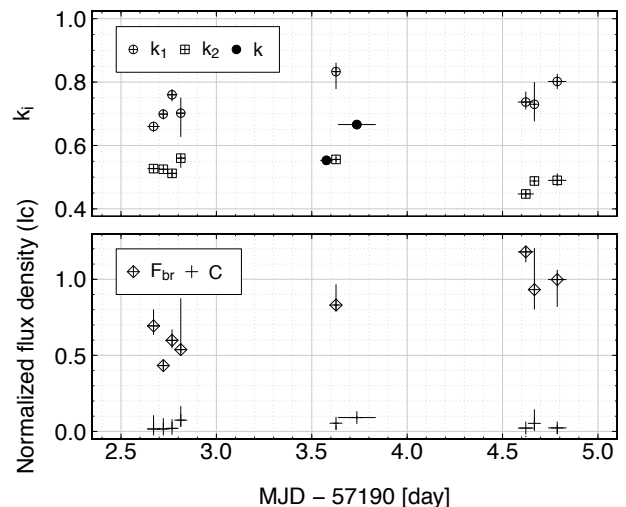


Fig. 5. The parameters derived by broken-linear model fitting to the flux-flux plots of  $g'$ -band and  $I_C$ -band.

in Fig.5. The slopes of the two segments of the broken linear model ( $k_1$  and  $k_2$ ) at each portions, we find that all of the  $k_1$  and  $k_2$  are clearly separated at  $\sim 0.6$  (Fig.5, the upper panel). For the two portions E and G, thus, we assigned the slope  $k$  to  $k_1$  if it is larger than 0.6, and to  $k_2$  otherwise. Additionally, we found in flux-flux plots (*e.g.* Fig.4) that the dynamic range of the flux variation in the component above the break is larger than that below. For example, the variation amplitude of the  $g'$ -band flux below and above the break are  $3\times$  and  $18\times$  the minimum flux respectively in period “B” (leftmost panel of Fig.4). It indicates that one variable component has quite large variability and dominates the optical variation when the component is much brighter than another one. Therefore, we named the components dominated at above the break as “highly-variable component” (HVC) and below that as “little-variable component” (LVC). The slope (or the flux ratio to  $g'$  band) of the LVC is varying in intra-day and has a redder color, whereas that of the HVC  $k_2$  is relatively stable but has long-term change and a bluer color.

#### 5.5 Decomposed Color-color Diagram

Fig.6 shows the color-color diagram for the decomposed components (HVC and LVC) constructed from the slopes of the broken-linear model. A variety of spectral indices of power law spectra should fall on the grey dashed line in the same way as Fig.2. The data points below the grey dashed line, therefore, corresponds to convex spectra and vice versa above the line.

Although spectral indices of the original data between  $g'$  and  $R_C$  reach down to  $-1.5$  as shown in Fig.2, those after the decomposition never reach  $-0.5$  as shown in Fig.5. It is due to the redder stable component (second term of the right hand side in Eq.5.3 and constant  $C$  in Table 3) especially prominent in the

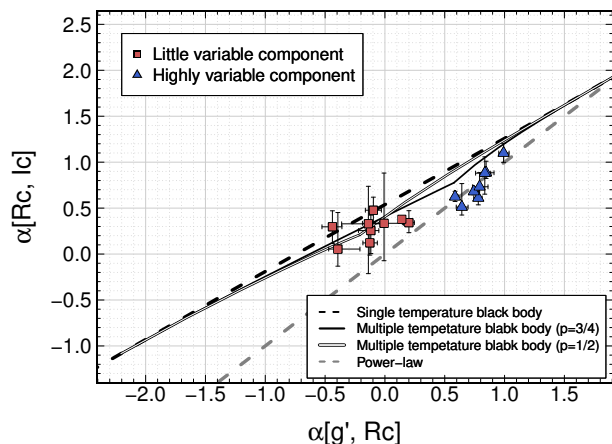


Fig. 6. Color-color diagram with the spectral indices between  $g'$ -band and  $R_C$ -band, and  $R_C$ -band and  $I_C$ -band, after the decomposition.

$R_C$ -band.

The spectral indices of the HVC lie on the gray dashed line indicating power-law spectra with variable its indices. On the other hand, those of the LVC exhibits softer spectra: spectral indices are consistent with those of the standard disk ( $p=3/4$ ) with the innermost temperature ( $T_{in}$ ) of typically  $\sim 1.5 \times 10^4$  K and 5000 K at the outer edge ( $T_{out}$ ), or the irradiated disk ( $p=1/2$ ) with  $T_{in} \gtrsim 2 \times 10^4$  K and  $T_{out} \lesssim 6500$  K.

## 6 Discussion

### 6.1 Optical Emission Components

We have shown that the optical variation is decomposed to two components; little-variable component (LVC) and highly-variable component (HVC). HVC has larger amplitude ( $\sim 5$ – $10$  times larger than that of LVC) and bluer color, and thus corresponds to “big-slow swings” mentioned in §3. On the other hand, LVC which has a redder spectrum corresponds to a characteristic behavior mentioned in §3 as “small-fast wiggles” as is similar to “heartbeat-type” oscillations observed by Kimura et al. (2016), considering its small amplitude and its dominance at the low flux phase.

Besides these components, Gandhi et al. (2016) reported rapid optical flux variability which sometimes are unresolved down to a time resolution of 24 milliseconds in the outburst. The rapid fluctuation is only present near the peak of the outburst on MJD 57199, but not on MJD 57193, 57194 and 57198. Although we are not sure whether sub-second flares were present in our data, it is reasonable to assume that the contribution from the sub-second flare is negligible because, (1) our dataset is in MJD 57192–57194, when the fast flares unlikely present, and (2) the variation amplitude of the sub-second flare ( $\sim 0.2$  mag, Gandhi et al. 2016) is adequately small relative to

that from the HVC or LVC ( $\sim 3$  mag and  $\sim 1$  mag). The sub-second optical flaring activity therefore would not affects our analysis and discussion below.

### 6.2 $H\alpha$ Emission Line

Gandhi et al. (2016) calculated the contribution of  $H\alpha$  emission line to the  $r'$ -band photometry by modeling the continuum spectrum under assumptions of spectral index ranging from +2 for a blue continuum to  $-2$  for a red continuum. The result is that  $H\alpha$  contributes about 10% to their  $r'$ -band flux at MJD=57199. If the  $H\alpha$  contribution is in  $R_C$ -band, the spectral index between  $R_C$ -band and  $I_C$ -band will be reduced by about 0.5, whereas that between  $g'$ -band and  $R_C$ -band increases by about 0.4. The data points in Fig.6 would then move toward lower-left region, and then almost all of them depart the power-law loci. If HVC or LVC contains the  $H\alpha$  line, therefore, the underlining continua of these components must have unnatural concave shapes at about every portions of our data set.

Additionally, Muñoz-Darias et al. (2015) found that flux of the  $H\alpha$  line was stable regardless of the variable continuum on MJD 57192. The  $H\alpha$  line, therefore, should be contained in the stable component (columns  $C$  in Table 3).

### 6.3 Origin of LVC

The time-scale of the LVC (*i.e.*, “small-fast wiggles”) about a few minutes, corresponding to the light crossing time of  $\sim 10^6$  Schwarzschild radius, constrains the upper limit for the optical-emission area of the accretion disk. It is roughly consistent with the radii where the disk can extend out,  $1.2 \times 10^{12}$  cm =  $4.4 \times 10^5$  Schwarzschild radius (Shahbaz et al. 1994) for the mass of the black hole  $M_{BH} \sim 9 M_{\odot}$ .

We found that spectral indices of LVC are consistent with those of a standard disk or an irradiated disk. However, a standard disk truncated at such a low innermost temperature ( $\sim 1.5 \times 10^4$  K) seems to be difficult to reconcile with the detection of a disk component in the soft X-ray region (Radhika et al. 2016 and Walton et al. 2016). For the origin of LVC, thus, the irradiated disk is favored. From the observed flux, the outer radius of the disk is evaluated to be  $\sim 3$ – $5 \times 10^5$  Schwarzschild radius. It is consistent with the size limit based on the timescale of LVC. The irradiated disk is therefore the most plausible source of the LVC.

We additionally note that the gradual brightening during MJD 57192 – 57195 (also reported by Kimura et al. 2016) is likely due to increase of the LVC. In the lower panel of Fig.5, the break flux density  $F_{br}$  increases day by day while the intercept  $C$  stays almost constant.  $F_{br}$  at MJD 57914 is about two times higher (corresponding to  $\sim 0.75$  mag lower) than that at MJD 57192. This means that the gradual brightening trend is mostly attributed to the increase of the average flux

of LVC, probably because the optical emitting region gradually moved outward as X-ray emission from the central region grew stronger.

#### 6.4 Origin of HVC

The decomposed color-color diagram shows that the spectrum of HVC is following power-law model with a spectral index of  $\sim 0.6$ – $1.0$ . This component has drastic amplitude of variation ( $\sim 5$ – $10$  times larger than that of LVC) within  $\sim 15$ – $50$  minutes, and thus corresponds to “big up-and-down swings” mentioned in §3. The rising time ( $T_r$ ) of flux is constantly longer than the decaying time ( $T_d$ ), while  $T_r$  had changed day by day; on MJD = 57192,  $T_r \sim 1$  hour is slightly longer than  $T_d \sim 30$  min, whereas on MJD = 57193,  $T_r > 4$  hour is apparently longer than  $T_d$ . Though, interestingly, the spectral index of HVC is almost stable for all of our data set. For interpreting power-law spectrum of HVC, synchrotron emission from the jet is conceivable firstly.

Martí et al. (2016) discussed about the possibility that the optical variation in flux and color is interpreted in an scenario based on the ejection of non-thermal emitting such as jet from radio to optical wavelengths. Recently, Shahbaz et al. (2016) and Lipunov et al. (2016) reported variable optical linear polarization, changing by  $\sim 1\%$  over a timescale of  $\sim 0.5$ – $1$  hour, after subtracting the contribution from interstellar dust between V404 Cyg and the Earth. The time-scale of the variation is consistent with that in our “big up-and-down swings”. Both of them concluded that the jet synchrotron emission is a viable candidate for the variable polarization. Furthermore, during this outburst V404 Cyg exhibited large variation in the radio (Tetarenko et al. 2015, Trushkin et al. 2015b), and its spectrum at MJD 57191.952 can be well described by power-law with spectral index  $\sim 0.65$  (Trushkin et al. 2015a). Therefore, a jet was likely to be present. Since the spectral break from optically thick regime to thin is expected to lie at  $\sim 1.4$ – $4.7 \times 10^{14}$  Hz (Shahbaz et al. 2016, Tanaka et al. 2016, and Itoh et al. 2016), the blue spectrum seen in HVC ( $\alpha \sim 0.5$ – $1.0$ ) is probably attributed to the transitioning spectrum from optically thick synchrotron spectrum to that of thin regime. The jet is therefore one of the strongest candidate of the origin of HVC.

Another possibility is the thermal cyclo-synchrotron emission as proposed for XTE J1118+480 (Merloni et al. 2000 and Kanbach et al. 2001) and V4641 Sgr (Uemura et al. 2002). The time-scale of the optical fluctuation in V4641 Sgr is similar to V404 Cygni (shorter than  $\sim 1$  hour), and moreover the self absorbed regime of the cyclo-synchrotron spectrum can produce the spectral index harder than  $\sim 0.6$ . The cyclo-synchrotron emission is also a possible mechanism of the power-law component (HVC).

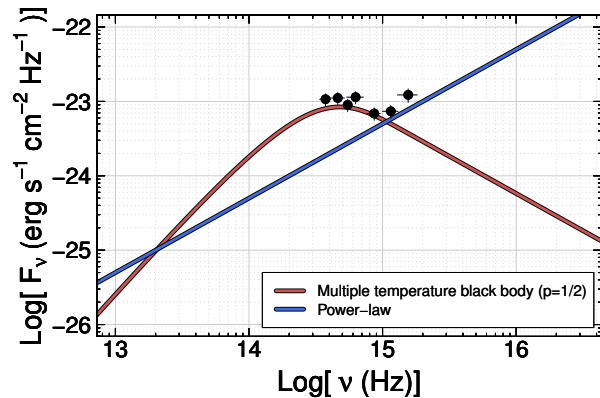


Fig. 7. SED from optical to UV with an irradiated disk spectrum (solid line) and power-law spectrum (dashed line) in MJD  $\sim 57194.61$  –  $57194.62$  (included in “H” period in Fig. 1).

#### 6.5 Origin of the stable component

As mentioned in §5.5, the stable component, namely a component not varying much in the time window of a flux-flux plot, is an underlying variable component prominently in the  $R_C$ -band (Tab.3, denoted as  $C$ ). Its time-scale of the variation, therefore, must be longer than  $\sim 1$  hour. Although we cannot determine the spectral shape, it is likely that  $H\alpha$  emission is contained in this component, because  $H\alpha$  strength seems to be more stable and almost continuum independent (Muñoz-Darias et al. 2015), and the flux of this component is prominent in the  $R_C$ -band which is including the wavelength of the line. These pieces of evidence, namely, the variation time scale longer than  $\sim 1$  hour and the possibility of the line contribution in  $R_C$ -band, suggest that the stable component is a disk or companion wind origin (e.g., Radhika et al. 2016, Rahoui et al. 2017). Its flux contribution is typically larger than  $\sim 5$ – $10\%$  (estimated by  $C/F_{br}$ ) in MJD 57192, and then gradually decrease toward  $\sim 2$ – $5\%$  as  $F_{br}$  grow up (mentioned in §6.3).

#### 6.6 SED from optical to UV

To confirm our interpretations discussed above, we tried to describe the spectral energy distribution (SED) from optical to ultraviolet with a power-law and a irradiated disk spectra. Constructed SEDs at MJD 57194.616 (included in “H” portion in Fig.1) are displayed in Fig.7. Four *Swift*/UVOT fluxes (V, U, UVW1, and UVW2) are obtained quasi-simultaneously with the optical bands within 12 mins. We ignored the flux of the stable component since its contribution is insignificant relative to LVC and HVC ( $\gtrsim 10$  times lower than that of the minimum flux we observed in these time windows). The solid line and the dashed line denote the irradiated disk spectrum (the outermost temperature  $T_{out} = 5 \times 10^3$  K with emitting size  $R = 4 \times 10^5 R_s$ ) and the power-law spectrum with an index  $\alpha = 1.0$  respec-



tively. Although we did not use the UVOT data to derive the spectral model, all data points appear to fit nicely with the two component model including the UV excess. Using the spectral analysis, we additionally confirmed the results from flux-flux plot (§5.4) that the optical variation with large amplitude are mostly attributed to HVC. When we fit the optical SED with the two component model with fixed disk temperature and fixed power-law index for each time window (A–J), normalizations of LVC was quite stable compared to those of the power-law components. This behaviors are consistent with the variability in “small-fast wiggles” and “big up-and-down swings”, respectively. On the other hand, the SED at dim phases seems to be affected by the stable component, which shows a redder spectrum than LVC. These consistencies strongly supports our interpretation.

Our result that the optical emission consists of two variable components and one stable component, has possibilities to give an interpretation for the characteristic flux variations between optical and X-ray pointed out by Kimura et al. (2016); although the amplitudes of the variations in X-ray and optical are generally correlated and it indicates that both X-ray and optical variations are reflected the same phenomena, the X-ray flux variations were always much larger than the optical ones. The smaller amplitude in the optical-band relative to X-ray is naturally interpreted by the “bias” (stable component) lying under the variable component (HVC and/or LVC) correlated with X-ray variation. In MJD  $\sim 57193.63$  (in “F” segment), for example, a rapid fading was observed simultaneously in optical and X-ray. However, its amplitude was quite different;  $\times 1/100$  in X-ray while  $\times 1/5$  in  $R_C$  band. The stable component contributes at least 2% and as much as 22% of the peak flux before the fading in the  $R_C$  band. We therefore can attribute the difference in fading amplitude of optical and X-ray to the stable component sustaining the optical flux.

## 7 Summary

In this work, we found that the optical emission of V404 Cygni in 2015 outburst can be decomposed to three components: the little-variable component (LVC), the highly-variable component (HVC), and the stable component, based on the analysis of the flux-flux plot which have a break and then is well represented by broken-liner expression.

The spectral indices of LVC and HVC on the color-color diagram indicate that LVC shows multi-temperature black body spectra with the disk with  $T(r) \propto r^{-1/2}$ , while HVC shows power-law spectra. The inner and outermost temperatures ( $T_{in/out}$ ) and the outermost radius of the irradiated disk are  $T_{in} \gtrsim 2.0 \times 10^4$  K,  $T_{out} \lesssim 6.5 \times 10^3$  K, and  $(3-5) \times 10^4$  Schwarzschild radii respectively. The gradual brightening trend of the light curves over MJD 57182–57194 ( $\sim 0.6$  mag) is

mostly attributed to this disk component. On the other hand, the HVC has a power-law index of 0.6–1.0. We proposed a non-thermal jet or thermal cyclo-synchrotron emission as its origin of the power-law component (HVC). For the origin of remaining stable component, we suggested a large scale disk or the companion star wind, on the basis of its stability and  $H\alpha$  line contribution suggested by its prominence in the  $R_C$ -band.

The decomposition of the optical flux variation into the two variable components based on the flux-flux plot analysis is supported by the analysis of the optical-UV spectral energy distribution, which can be described by the combination of an irradiated disk and a power-law component. We further find that observed optical spectra at different epochs can be reconstructed by the two spectral components with different time variability, “small-fast wiggles” of the disk and “big-slow swings” of the power-law component.

Additionally, we showed that the difference in variation amplitudes in optical and X-ray, which are generally correlated, can be interpreted with the flux contribution from stable component; it lies under the variable component and sustains the optical flux.

## Acknowledgments

We thanks to the referee Dr. Josep Martí for helpful comments and suggestions that improved the paper. Part of this work was financially supported by the Grant-inAid for JSPS Fellows for young researchers (Y.T.) and by Ministry of Education, Culture, Sports, Science and Technology of Japan (MEXT), Grant-in-Aid No.14GS0211, 19047003 and 24103002 (N.K.). We acknowledge support for MITSuME Telescope at Akeno by the Inter-University Research Program of the Institute for Cosmic Ray Research, University of Tokyo. This work was supported by the Optical and Near-infrared Astronomy Inter-University Cooperation Program and the JSPS-NSF PIRE Program.

## References

- Barthelmy, S. D., D’Ai, A., D’Avanzo, P., et al., 2015, GCN Circular, 17929, 1
- Belloni, T., Klein-Wolt, M., Méndez, M., van der Klis, M., & van paradijs, J., 2000, A&A, 355, 271
- Coriat, M., Fender, R. P., & Dubus, G., 2012, MNRAS, 424, 1991
- Casares, J., Charles, P. A. & Naylor, T., 1992, Nature, 355, 614
- Eikenberry, S. S., Matthews, K., Morgan, E. H., 1998, ApJ, 494, L61
- Fender, R. & Belloni, T., 2004, ARA&A, 42, 317
- Ferrigno, C., Fotopoulou, S., Domingo, A., et al., 2015, The Astronomer’s Telegram, 7662, 1
- Gandhi, P., Littlefair, S. P., Hardy, L. K., et al., 2016, MNRAS, 459, 554
- Itoh, R. and Tanaka, Y. T. and Kawabata, K. S. et al., 2016, ArXiv e-prints, 1612.07513
- Kanbach, G., Straubmeier, C., Spruit, H. C., et al., 2001, Nature, 414, 180
- Khargharia, J., Froning, C. S., & Robinson, E. L., 2010, ApJ, 716, 1105
- Kimura, M., Isogai, K., Kato, T., et al., 2016, Nature, 529, 54
- King, A. R. & Ritter, H., 1998, MNRAS, 293, L42
- King, A. L., Miller, J. M., Raymond, J. et al., 2015, ApJL, 813, L37

- Kitamoto, S., Tsunemi, H., Miyamoto, S., et al., 1989, *Nature*, 342, 518
- Kotani, T., Kawai, N., Yanagisawa, K., et al., 2005, *Nuovo Cimento C Geophysics Space Physics C*, 28, 755
- Landolt, A. U., 1992, *AJ*, 104, 340
- Lipunov, V. M., Gorbvskoy, E., Kornilov, V. et al., 2016, *ApJ*, 833, 198
- Makino, F., Wagner, R. M., Starrfield, S., et al., 1989, *IAU Circ.*, 4786
- Merloni, A., Di Matteo, T., & Fabian, A. C., 2000, *MNRAS*, 318, L15
- Martí, J., Luque-Escamilla, P. L. and García-Hernández, M. T., 2016, *A&A*, 586, A58
- Miller-Jones, J. C. A., Jonker, P. G., Nelemans, G., et al., 2009, *MNRAS*, 394, 1440
- Mineshige, S., Hirano, A., Kitamoto, S., et al., 1994, *ApJ*, 426, 308
- Mink, D. J., 1997, *Astronomical Society of the Pacific Conference Series*, 125, 249
- Motch, C., Ricketts, M. J., Page, C. G., et al., 1983, *A&A*, 119, 171
- Muñoz-Darias, T., Mata Sanchez, D., & Casares, J., 2015, *The Astronomer's Telegram*, 7669, 1
- Muñoz-Darias, T., Casares, J., Mata Sánchez, D., et al., 2016, *Nature*, 534, 75
- Natalucci, L., Flocchi, M., Bazzano, A. et al., 2015, *ApJL*, 813, L21
- Negoro, H., Matsumitsu, T., Mihara, T., et al., 2015, *The astronomer's Telegram*, 7646, 1
- Noda, H., Makishima, K., Yamada, S., et al., 2014, *ApJ*, 793, 2
- O'Donnell, J. E., 1994, *ApJ*, 422, 158
- Ponti, G., Miniutti, G., Cappi, M., et al., 2006, *MNRAS*, 368, 903
- Radhika, D., Nandi, A., Agrawal, V. K. et al., 2016, *MNRAS*, 462, 1834
- Rahoui, F. and Tomsick, J. A. and Gandhi, P. et al., 2017, *MNRAS*, 465, 4468
- Rodriguez, J., Cadolle Bel, M., Alfonso-Garzón, J. et al., 2015, *A&A*, 581, L9
- Roques, J.-P., Jourdain, E., Bazzano, A. et al., 2015, *ApJL*, 813, L22
- Shahbaz, T., Ringwald, F. A., Bunn, J. C., et al., 1994, *MNRAS*, 271, L10
- Shahbaz, T., Dhillon, V. S., Marsh, T. R. et al., 2003, *MNRAS*, 346, 1116
- Shahbaz, T., Russell, D. M., Covino, S. et al., 2016, *MNRAS*, 463, 1822
- Shakura, N. I., & Sunyaev, R. A., 1973, *A&A*, 24, 337
- Shimokawabe, T., Kawai, N., Kotani, T., et al., 2008, *American Institute of Physics Conference Series*, 1000, 543
- Smith, J. A., Tucker, D. L., Kent, S. et al., 2002, *AJ*, 123, 2121
- Tanaka, Y., & Shibazaki, N., 1996, *ARA&A*, 34, 607
- Tanaka, Y. T., Itoh, R., Umemura, M., et al., 2016, *ApJ*, 823, 35
- Taylor, R. D., Uttley, P., & McHardy, I. M., 2003, *MNRAS*, 342, L31
- Tetarenko, A., Sivakoff, G. R., Gurwell, M. A., et al., 2015, *The Astronomer's Telegram*, 7661, 1
- Trushkin, S. A., Nizhelskij, N. A. & Tybulev, P. G., 2015, *The Astronomer's Telegram*, 7667, 1
- Trushkin, S. A., Nizhelskij, N. A. & Tybulev, P. G., 2015, *The Astronomer's Telegram*, 7716, 1
- Uemura, M., Kato, T., Matsumoto, K., et al., 2000, *PASJ*, 52, L15
- Uemura, M., Kato, T., Ishioka, R., et al., 2002, *PASJ*, 54, L79
- Uttley, P., McHardy, I. M., & Vaughan, S., 2005, *MNRAS*, 359, 345
- Walton, D. J., Mooley, K., King, A. L., et al., 2016, *ArXiv e-prints*, 1609.01293
- Yatsu, Y., Kawai, N., Shimokawabe, T., et al., 2007, *Physica E Low-Dimensional Systems and Nanostructures*, 40, 434
- Życki, P. T., Done, C., & Smith, D. A., 1999, *MNRAS*, 309, 561

**Table 1.** The information of V404 Cyg, reference stars, and photometric standard stars.

Objects		Magnitude			
Name	Attribution	RA, Dec (J2000)	$g'$	$R_C$	$I_C$
V404 Cyg	Target	(20:24:03.83, +33:52:02.2)			
SA111-1925	Standard	(19:37:28.62, +00:25:03.1)	12.545	12.167	11.914
SA111-1965		(19:37:41.55, +00:26:50.9)	12.272	10.468	9.591
SA111-1969		(19:37:43.29, +00:25:48.6)	11.370	9.205	7.983
SA111-2039		(19:38:04.58, +00:32:12.8)	13.064	11.656	10.967
SA111-2088		(19:38:21.25, +00:31:00.4)	13.992	12.305	11.487
SA111-2093		(19:38:23.44, +00:31:25.7)	12.812	12.168	11.771
SA112-223		(20:42:14.58, +00:08:59.7)	11.606	11.151	10.877
SA112-250		(20:42:26.38, +00:07:42.4)	12.314	11.778	11.455
SA112-275		(20:42:35.43, +00:07:20.2)	10.488	9.258	8.689
SA112-805		(20:42:46.74, +00:16:08.4)	12.087	12.023	11.948
SA112-822		(20:42:54.90, +00:15:01.9)	12.028	10.991	10.489
ref1	Reference	(20:24:07.17, +33:50:51.9)	$13.045 \pm 0.007$	$12.416 \pm 0.004$	$12.011 \pm 0.004$
ref2		(20:23:53.39, +33:52:24.2)	$13.800 \pm 0.007$	$12.762 \pm 0.005$	$12.249 \pm 0.008$
ref3		(20:24:08.87, +33:54:38.3)	$13.403 \pm 0.008$	$12.743 \pm 0.006$	$12.341 \pm 0.008$
ref4		(20:23:56.48, +33:48:17.2)	$12.564 \pm 0.008$	$12.224 \pm 0.004$	$11.948 \pm 0.005$
ref5		(20:24:25.13, +33:51:56.1)	$13.247 \pm 0.007$	$12.854 \pm 0.006$	$12.550 \pm 0.007$

**Table 2.** Log of optical observations.

MJD	Duration [minute]	Exposure [sec]	Number [frame]	Location
57192.55102 – 57192.56430	19.1	60	15	Ishigaki
57192.56605 – 57192.57936	19.2	30	30	Ishigaki
57192.58012 – 57192.69439	164.5	20	333	Ishigaki
57192.70261 – 57192.83388	189.0	10	572	Ishigaki
57193.54567 – 57193.60504	85.5	10	278	Ishigaki
57193.60549 – 57193.83348	328.3	5	887	Ishigaki
57194.54989 – 57194.83326	408.1	20	577	Ishigaki
57194.55391 – 57194.74250	271.6	30	101	Akeno

**Table 3.** Derived parameters by broken-linear model fit to flux-flux plots.

MJD	Broken-linear model ( $g'$ and $R_C$ )				Broken-linear model ( $g'$ and $I_C$ )			
	$k_1$	$C$	$F_{br}$	$k_2$	$k_1$	$C$	$F_{br}$	$k_2$
57192.6456 – 57192.7012 (A)	$0.756^{+0.012}_{-0.010}$	$0.111^{+0.007}_{-0.008}$	$1.292^{+0.098}_{-0.090}$	$0.639^{+0.007}_{-0.006}$	$0.660^{+0.011}_{-0.016}$	$0.088^{+0.011}_{-0.008}$	$1.286^{+0.157}_{-0.083}$	$0.527^{+0.006}_{-0.010}$
57192.7012 – 57192.7423 (B)	$0.824 \pm 0.016$	$0.081 \pm 0.004$	$0.788^{+0.070}_{-0.056}$	$0.646^{+0.003}_{-0.004}$	$0.699^{+0.014}_{-0.016}$	$0.069 \pm 0.004$	$0.794^{+0.066}_{-0.051}$	$0.525 \pm 0.003$
57192.7423 – 57192.7928 (C)	$0.831^{+0.014}_{-0.015}$	$0.081 \pm 0.004$	$1.249^{+0.132}_{-0.109}$	$0.637^{+0.011}_{-0.013}$	$0.760^{+0.017}_{-0.020}$	$0.058^{0.009}_{-0.006}$	$1.130^{+0.121}_{-0.086}$	$0.512^{+0.010}_{-0.013}$
57192.7928 – 57192.8339 (D)	$0.803^{+0.042}_{-0.038}$	$0.107^{+0.022}_{-0.028}$	$1.023^{+0.069}_{-0.195}$	$0.665^{+0.009}_{-0.010}$	$0.702^{+0.048}_{-0.074}$	$0.091^{+0.042}_{-0.036}$	$0.828^{+0.723}_{-0.028}$	$0.560^{+0.007}_{-0.029}$
57193.5459 – 57193.6083 (E)	–	–	< 2.420	$0.665 \pm 0.007$	–	–	< 2.420	$0.553 \pm 0.007$
57193.6150 – 57193.6390 (F)	$0.898^{+0.020}_{-0.048}$	$0.055^{+0.040}_{-0.024}$	$1.407^{+0.207}_{-0.010}$	$0.676^{+0.004}_{-0.006}$	$0.833^{+0.027}_{-0.054}$	$-0.015^{+0.043}_{-0.028}$	$1.397^{+0.173}_{-0.044}$	$0.556 \pm 0.005$
57193.6390 – 57193.8335 (G)	$0.769^{+0.003}_{-0.004}$	$0.138^{+0.008}_{-0.007}$	> 2.324	–	$0.666 \pm 0.004$	$0.091^{+0.009}_{-0.008}$	> 2.324	–
57194.5820 – 57194.6617 (H)	$0.829^{+0.025}_{-0.016}$	$0.011^{+0.039}_{-0.060}$	$2.596^{+0.022}_{-0.064}$	$0.601^{+0.007}_{-0.008}$	$0.737^{+0.032}_{-0.026}$	$-0.057^{+0.053}_{-0.075}$	$2.591^{+0.026}_{-0.057}$	$0.447 \pm 0.008$
57194.6617 – 57194.6722 (I)	$0.834^{+0.054}_{-0.039}$	$0.128^{+0.035}_{-0.070}$	$1.836^{+0.310}_{-0.129}$	$0.627^{+0.005}_{-0.012}$	$0.730^{+0.069}_{0.053}$	$0.090^{+0.048}_{-0.089}$	$1.801^{+0.308}_{-0.146}$	$0.488^{+0.005}_{-0.009}$
57194.7404 – 57194.8330 (J)	$0.910^{+0.023}_{-0.021}$	$0.043^{+0.032}_{-0.036}$	$1.966^{+0.052}_{-0.113}$	$0.629^{+0.014}_{-0.009}$	$0.802 \pm 0.023$	$0.018 \pm 0.035$	$1.990^{+0.006}_{-0.181}$	$0.490^{+0.021}_{-0.017}$